Supplementry Information for "Emergence of flat bands via orbital-selective electron correlations in Mn-based kagome metal"

I. EXPERIMENTAL DETAILS

A. Sample growth, transport and magnetic characterizations

Single crystals of SMAS were grown by a self-flux method. The Sc, Mn, Al, and Si elements with a molar ratio 3:3:30:5 were ground and loaded into an alumina crucible. Then, the crucible was inserted inside a quartz tube and sealed under high-purity argon. The tube was heated to 1150 °C, kept at that temperature for 24 h, and subsequently cooled to 750 °C for 200 h. The single crystals were isolated by centrifugation. The magnetic susceptibility and magnetization were measured with a superconducting quantum interference device vibrating sample magnetometer (SQUID VSM) (Quantum Design, USA) in the temperature range of 1.8-300 K and the field range of $\mu_0 H$ = 0-7 T. Electrical resistivity measurements were carried out with a conventional four-point schema using a Quantum Design physical property measurement system (PPMS).

B. Nuclear magnetic resonance measurement

^{27}Al (gyromagnetic ratio γ_N = 11.0943 MHz/T) NMR experiments were conducted using a home-made NMR spectrometer (MagRes) and an Oxford Teslatron PT superconducting magnet in the temperature range of 2-150 K. To record ^{125}Al NMR spectra, we adopted a standard Hahn-echo (spin-echo) sequence with a $\pi/2$ pulse length of 2 μs. In the process of tracking all peaks, we varied a resonance frequency at a fixed magnetic field of $\mu_0 H$ = 6 T. The spin-lattice ($1/T_1$) and spin-spin relaxation rates ($1/T_2$) were measured with the standard saturation recovery and the Hahn echo method with twenty saturation pulse train.

C. Optical spectroscopy

We measured the reflectance of SMAS in a wide spectral range from 40 to 35000 cm^{-1} at various selected temperatures between 8 and 300 K using a commercial spectrometer Vertex 80v (Bruker, Germany) and a continuous liquid helium flow cryostat. To obtain accurate reflectance spectra, we used an *in-situ* metal evaporation method [1]. In this metal evaporation method, Au is used for far and mid-infrared regions, and Al is used for near-infrared and visible regions. The measured reflectance spectra at various temperatures are shown in Fig. 1. We observed that the overall level of the reflectance is quite high above 40% up to 35000 cm^{-1} and a sharp plasma edge is located near 1500 cm^{-1}. In the inset, we display the reflectance at 100 cm^{-1} as a function of temperature, where we observe non-monotonic temperature-dependent behavior. There is a broad peak near 30 K, which is similar temperature-dependent behavior of the measured DC resistivity.

II. COMPUTATIONAL DETAILS

A. Density functional theory

First principles electronic structure calculations were carried out, employing more accurate full potential-based WIEN2k code [2]. A non-shifted 10×10×8 k-grid was chosen to sample the hexagonal Brillouin zone. The muffin-tin radii of Sc, Mn, Al, and Si were set to 2.5, 2.5, 1.94, and 2.21 a.u., respectively. The LAPW basis included 3d, 4s for Sc and Mn; 3s, 3p for Al and Si elements. For self-consistent electronic cycles, the planewave cutoff was taken to 9, yielding 5162 for each k-point. Additionally, DFT+U calculations were performed using rotationally invariant Dudarev approach [3] with effective Coulomb repulsion parameter U ($U_{\rm eff}$=4, 8 eV).

B. Dynamical mean field theory

LDA+DMFT calculations were performed employing embedded DMFT code [4, 5], interfaced with the full potential based WIEN2k package [2]. A similar size of k-grid 10×10×8, as used in DFT calculations, was employed and $RK_{\rm max}$ was set to 9. The quantum impurity problem was solved in the correlated subspace of Mn d-orbitals, using hybridization-expansion continuous-time quantum Monte Carlo (CT-HYB) method [6, 7]. For each charge self-consistent DMFT iteration, 192×10^9 Monte Carlo steps were performed. The DMFT calculations were carried out for a wide range of temperature 116-2000 K. For each temperature, 50 DMFT charge cycles were run. The calculations were performed using both Ising as well as rotationally invariant full Coulomb interactions. Four different values of on-site Coulomb (U= 4, 6, 8, 10 eV) and two different choices of Hund's ($J_{\rm H}$ = 0.8, 1.0 eV) parameters were taken in the calculations. Most of the calculations results were obtained using ($U, J_{\rm H}$)=(8, 0.8) eV with full Coulomb interaction.

III. OPTICAL CONDUCTIVITY

The optical conductivity was obtained from the measured reflectance (see Fig. 1) by using the Kramers-Kronig analysis [8, 9]. To perform the Kramers-Kronig analysis, the reflectance spectrum in a finite spectral range must be extrapolated to zero and infinity. For extrapolation to zero frequency, we used the Hagen-Rubens relation, i.e., $1 - R(\omega) \propto \sqrt{\omega}$. For extrapolation to infinity, we used $R(\omega) \propto \omega^{-1}$ from the

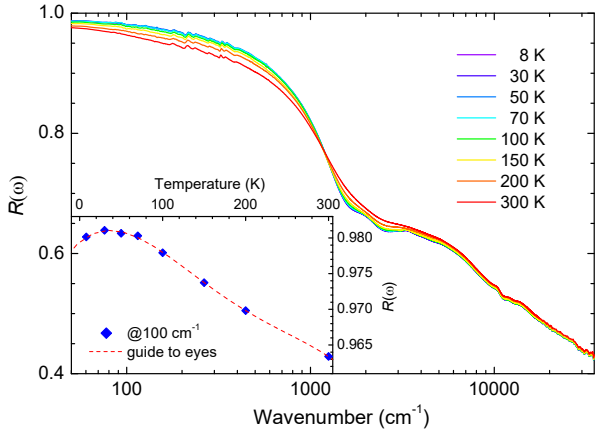

FIG. 1. Measured reflectance spectra of SMAS at various selected temperatures. In the inset, the reflectance at 100 cm^{-1} is shown as a function of temperature.

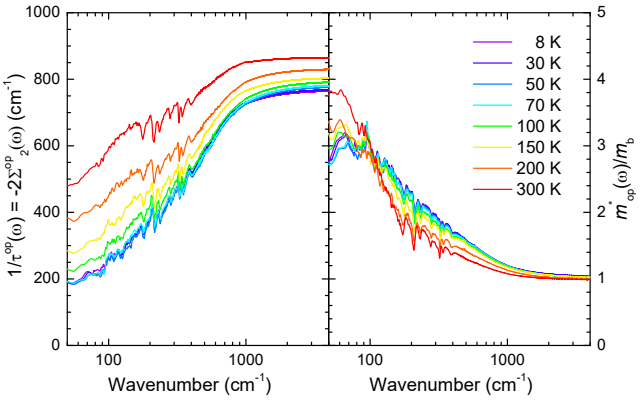

FIG. 2. Optical scattering rates and effective masses of SMAS at various temperatures.

highest data point to 10^6 cm^{-1}, and then above 10^6 cm^{-1}, we assumed the free-electron behavior, *i.e.*, $R(\omega) \propto \omega^{-4}$. The optical conductivities at various temperatures obtained using the Kramers-Kronig analysis are shown in Fig. 7(a) in the main text. There are many sharp infrared-active phonon absorption peaks below 500 cm^{-1}. We obtained the DC conductivity from extrapolation to zero frequency of the optical conductivity. In the inset, the DC resistivity obtained using the extrapolation and the measured DC one are shown. They are consistent with each other.

Now, to obtain information on the correlations between charge carriers, we used the extended Drude model formalism. In the extended Drude model, the complex optical conductivity can be expressed as follows [10, 11].

$$\tilde{\sigma}(\omega) = i\frac{\Omega_p^2}{4\pi}\frac{1}{\omega + \left[-2\tilde{\Sigma}^{\rm op}(\omega)\right]}, \qquad (1)$$

where Ω_p is the plasma frequency of itinerant charge carriers and $-2\tilde{\Sigma}^{\rm op}(\omega)$ is the complex optical self-energy, which may carry information on the correlations between itinerant charge carriers. The imaginary part, $\mathrm{Im}[-2\Sigma_2^{\rm op}(\omega)]$ is the same as the optical scattering rate $(1/\tau^{\rm op}(\omega))$ and the corresponding real part is associated with the optical effective mass $(m^*_{\rm op}(\omega)/m_{\rm b})$, *i.e.*, $\mathrm{Re}[-2\Sigma_1^{\rm op}(\omega)] = \left(\frac{m^*_{\rm op}(\omega)}{m_{\rm b}} - 1\right)\omega$, where $m_{\rm b}$ is the band mass. We obtained the plasma frequency by excluding the interband transitions above 1500 cm^{-1}. The resulting plasma frequency is 14890 cm^{-1}. Here, we first removed the interband transitions from the optical conductivity and then obtained the optical scattering rates and effective masses using the extended Drude formalism. The optical scattering rates and effective masses $\left(\frac{m^*_{\rm op}(\omega)}{m_{\rm b}}\right)$ at various temperatures are shown in Fig. 2. The value of the optical effective mass at zero frequency is the effective mass with respect to the band mass, *i.e.*, $\frac{m^*_{\rm op}(0)}{m_{\rm b}} = \frac{m^*}{m_{\rm b}}$. The effective mass is roughly in a range from 2.8 to 3.8. It is worth noting that these values are dependent on the plasma frequency.

IV. ^{27}AL NUCLEAR MAGNETIC RESONANCE RESULTS

Fig. 3(a) shows the thermal evolution of ^{27}Al NMR spectra of SMAS. We observe five NMR lines, which stem from the quadrupole interaction of the $I = 5/2$ nonspherical nucleus with its electronic surroundings. Figs. 3(b) plots the Knight shift K versus $\chi(T)$ for the central line P_3. Here, $K(T)$ is defined by $K(\mathrm{ppm}) = (\nu_{\rm P3} - \nu_{\rm Larmor})/\nu_{\rm Larmor}$, where $\nu_{\rm Larmor}$ is the Larmor frequency corresponding to an external field of $\mu_0 H = 6$ T. Using the Clogston-Jaccarino K-χ plot, we estimate the hyperfine interaction $A = 6.57\mathrm{mT}/\mu_{\rm B}$ between the ^{27}Al nuclear spins and the Mn electron spins. Figures 3(c) and (d) exhibit the temperature dependence of the nuclear spin-spin relaxation rate $1/T_2$ and the nuclear spin-lattice relaxation rate $1/T_1$, respectively. As the temperature is lowered from $T = 120$ K, $1/T_2$ decreases gradually and then, forms a minimum at 30 K, and finally shows a steep increase towards $T = 0$ K. Noteworthy is that $\rho(T)$ displays the minimum at the same temperature, implying that the $1/T_2$ and $\rho(T)$ anomalies below 30 K are due to the buildup of ferromagnetic correlations.

The temperature dependence of $1/T_1$ follows the so-called Korringa law in the temperature range investigated with $T_1T = 44.8833 \pm 0.24882$ s·K for $T < 40$ K and $T_1T = 40.1159 \pm 0.19825$ s·K for $T > 40$ K. Using the value for the Knight shift and $S = (\gamma_{\rm e}/\gamma_{\rm n})^2(h/8\pi^2 k_{\rm B}) = 3.89 \times 10^{-6}$ s·K for ^{27}Al, we evaluate the Korringa ratio $R = K^2T_1T/S \approx 0.05$ at $T = 2$ K, much smaller than the unity. This indicates that $1/T_1$ is not dominated by a scattering mechanism with *s*-type conduction electrons at the Fermi surface. Further, the small change of the Korringa ratio through 40 K suggests the alteration of a scattering mechanism.

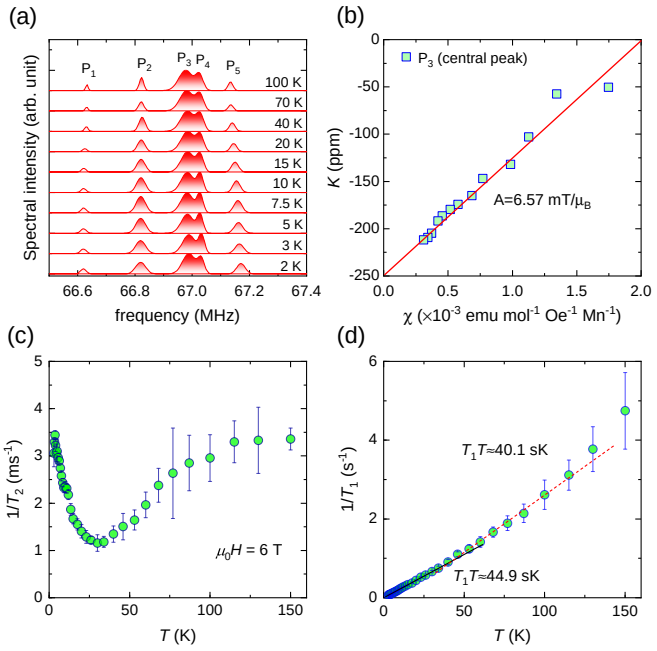

FIG. 3. Temperature dependence of ^{27}Al NMR spectra of SMAS measured at $\mu_0 H = 6$ T. (b) Plot of the Knight shift vs the static magnetic susceptibility. The solid line is the fit to the Clogston-Jaccarino relation. Temperature dependence of (c) the nuclear spin-spin relaxation rate $1/T_2$ and the spin-lattice relaxation rate $1/T_1$. The solid and dashed lines are fits to the Korringa relation T_1T=constant.

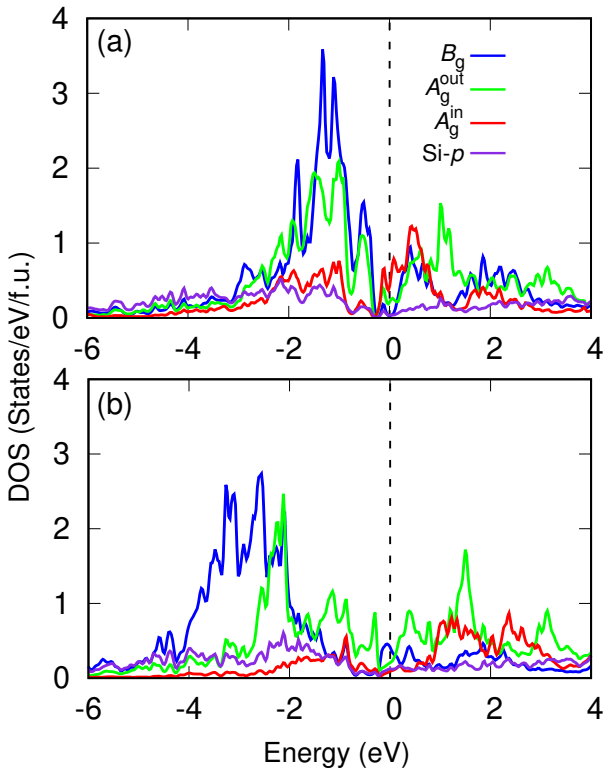

FIG. 4. (a), (b) PDOS of SMAS from non-spin-polarized LDA+U calculations with Mn B_g (blue), A_g^{out} (green), A_g^{in} (red), and Si p (violet) orbitals for U=4, 8 eV, respectively.

V. ELECTRONIC STRUCTURE FROM NON-SPIN-POLARIZED LDA+U CALCULATIONS

Fig. 4 demonstrates the effect of static electron correlation on SMAS within the LDA+U formalism. The spin-polarized calculation results are shown for two different values of $U_{\rm eff}$=4, 8 eV, where both results converge into non-spin-polarized solutions. Note that, up to $U_{\rm eff}$ = 10 eV no magnetic solution is obtained in our LDA+U calculations. Comparing the PDOS without (see Fig. 3 in the main text) and with U, we find that inclusion of U on Mn d orbitals pushes occupied d states downward, affecting the Mn d and Si p hybridization. In Fig. 4(a), occupied B_g and A_g peaks in the PDOS are located around −1 eV. As U is increased from 4 to 8 eV, B_g peaks are further pushed downward and are now located around −3 eV, lying lower in energy than A_g^{out}.

VI. GAP OPENING AT DIRAC CONE AND FURTHER BAND FLATTENING VIA SPIN-ORBIT COUPLING

Despite the strength of SOC at the Mn site is weak, SOC still can affect electronic properties significantly when bands are nearly degenerate and bandwidth is small. Fig. 5 summarizes the SOC effect on DMFT spectral function. The results are obtained for (U, J_H)=(4, 0.8) and (10, 0.8) eV at 116 K using Ising-type Coulomb interactions. Fig. 5(a) shows the presence of the dispersive B_g-bands along the K−Γ direction with a bandwidth of ∼ 0.30 eV. Inclusion of SOC induces a small gap between Dirac point and flat band at K point as shown in Fig. 5(b). Because of admixture of other states in the presence of SOC, bandwidth of nodal surface band slightly enhances.

The most striking feature of the spectral function at U = 10 eV is the presence of a nearly flat band just below E_F, lying along the high symmetry path K−Γ. Without SOC, such a flat band state at the k_z = 0 plane was present below E_F (see Fig. 5(c)). Including the SOC removes the Dirac points located close to E_F at K and opens up a gap of 10 meV, which makes the almost-flat band even flatter along the K−Γ direction. On the other hand, because of the weak strength of SOC, the k_z = π nodal surface bands are almost unaffected. The SOC-induced band anticrossings at K may result in significant Berry-phase effects like spin-Hall responses.

The correlation-induced flat bands and their topological nature in the presence of SOC might make SMAS a promising candidate to see a signature of spin Hall or anomalous Hall conductivity, as reported in other kagome metals CoSn [12, 13] or YMn_6Sn_6 [14]. Further, we speculate that this system might exhibit negative magnetoresistance at low temperatures. It has been suggested in the literature that the presence of flat bands close to the E_F induces ferromagnetic fluctuations that increase the scattering probability in a kagome plane. Indeed, our isothermal magnetization measurement at 2 K confirms this notion. At very low temperatures, an application of an external magnetic field might therefore suppress

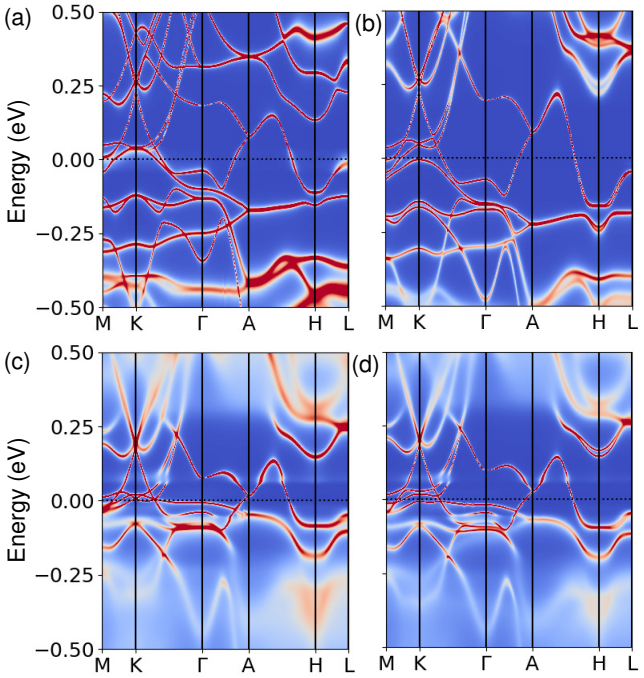

FIG. 5. (a)-(b) Close-up view of spectral function without and with SOC for $(U, J_{\rm H})$=(4, 0.8) eV, and (c)-(d) (10, 0.8) eV at T=116 K using Ising-type Coulomb interaction, respectively.

low-energy magnetic excitation to give rise to negative magnetoresistance [15, 16].

VII. EXACT AND OTHER CHOICE OF NOMINAL OCCUPANCY IN NOMINAL DOUBLE COUNTING SCHEME

The choice of double-counting scheme affects DMFT results and conclusions. In the main text, we presented results with employing the nominal double-counting scheme [4] with the nominal charge of $n = 5.0$. Figs. 6 and 7 summarize the results with $n = 4.5$ and 5.5, respectively. At $n = 4.5$ the flat band is pushed up to $E_{\rm F}$ and more strongly renormalized (Fig. 6). On the other hand, as n is increased to 5.5, the flat band is pushed downward and overall feature of electron correlations is significantly weakened (Fig. 7). At $n = 5.5$, the spectral function with $U = 4$ eV is very similar to the band dispersion calculated from simple DFT (see Fig. 3(a)-(c) in the main text for comparison).

Because the results critically depend on the choice of nominal charge, the results need to be tested with employing a parameter-free double-counting scheme. Hence, we checked our results using an exact double-counting scheme [17]. Fig. 8 shows the spectral function with the exact double-counting scheme, with the choice of $(U, J_{\rm H})$=(8, 0.8) eV and full Coulomb interaction at $T = 300$ K. The result looks very similar to the one from the nominal double-counting scheme with $n = 5.0$ (see Fig. 4(c) in the main text), where the d-orbital occupancy converges to 5.34.

[1] C. C. Homes, M. Reedyk, D. A. Cradles, and T. Timusk, Technique for measuring the reflectance of irregular, submillimeter-sized samples, Appl. Opt. **32**, 2976 (1993).

[2] P. Blaha, K. Schwarz, G. K. H. Madsen, D. Kvasnicka, J. Luitz, R. Laskowski, F. Tran, and L. D. Marks, *WIEN2k: An Augmented Plane Wave plus Local Orbitals Program for Calculating Crystal Properties* (Vienna University of Technology, Austria, 2018).

[3] S. L. Dudarev, G. A. Botton, S. Y. Savrasov, C. J. Humphreys, and A. P. Sutton, Electron-energy-loss spectra and the structural stability of nickel oxide: An LSDA+U study, Phys. Rev. B **57**, 1505 (1998).

[4] K. Haule, C.-H. Yee, and K. Kim, Dynamical mean-field theory within the full-potential methods: Electronic structure of $CeIrIn_5$, $CeCoIn_5$, and $CeRhIn_5$, Phys. Rev. B **81**, 195107 (2010).

[5] K. Haule, Structural predictions for correlated electron materials using the functional dynamical mean field theory approach, J. Phys. Soc. Japan **87**, 041005 (2018).

[6] P. Werner, A. Comanac, L. de' Medici, M. Troyer, and A. J. Millis, Continuous-time solver for quantum impurity models, Phys. Rev. Lett. **97**, 076405 (2006).

[7] K. Haule, Quantum Monte Carlo impurity solver for cluster dynamical mean-field theory and electronic structure calculations with adjustable cluster base, Phys. Rev. B **75**, 155113 (2007).

[8] F. Wooten, *Optical Properties of Solids* (Academic, New York, 1972).

[9] D. B. Tanner, *Optical effects in solids* (Cambridge Univ. Press, 2019).

[10] W. Götze and P. Wölfle, Homogeneous dynamical conductivity of simple metals, Phys. Rev. B **6**, 1226 (1972).

[11] J. Hwang, T. Timusk, and G. D. Gu, High-transition-temperature superconductivity in the absence of the magnetic-resonance mode, Nature **427**, 714 (2004).

[12] M. Kang, S. Fang, L. Ye, H. C. Po, J. Denlinger, C. Jozwiak, A. Bostwick, E. Rotenberg, E. Kaxiras, J. G. Checkelsky, and R. Comin, Topological flat bands in frustrated kagome lattice CoSn, Nat. Commun. **11**, 4004 (2020).

[13] Z. Liu, M. Li, Q. Wang, G. Wang, C. Wen, K. Jiang, X. Lu, S. Yan, Y. Huang, D. Shen, J.-X. Yin, Z. Wang, Z. Yin, H. Lei, and S. Wang, Orbital-selective Dirac fermions and extremely flat bands in frustrated kagome-lattice metal CoSn, Nat. Commun. **11**, 4002 (2020).

[14] M. Li, Q. Wang, G. Wang, Z. Yuan, W. Song, R. Lou, Z. Liu, Y. Huang, Z. Liu, H. Lei, Z. Yin, and S. Wang, Dirac cone, flat band and saddle point in kagome magnet YMn_6Sn_6, Nat. Commun. **12**, 3129 (2021).

[15] R. Arita, K. Kuroki, and H. Aoki, Electron-correlation-originated negative magnetoresistance in a system having a partly flat band, Phys. Rev. B **61**, 3207 (2000).

[16] J. Zhang, T. Yilmaz, J. W. R. Meier, J. Y. Pai, J. Lapano, H. X. Li, K. Kaznatcheev, E. Vescovo, M. B. A. Huon, T. Z. Ward, B. Lawrie, R. G. Moore, H. N. Lee, Y. L. Wang, H. Miao, and B. Sales, Flat band induced negative magnetoresistance in multi-orbital kagome metal, arXiv arXiv:2105.08888 (2021).

[17] K. Haule, Exact double counting in combining the dynamical

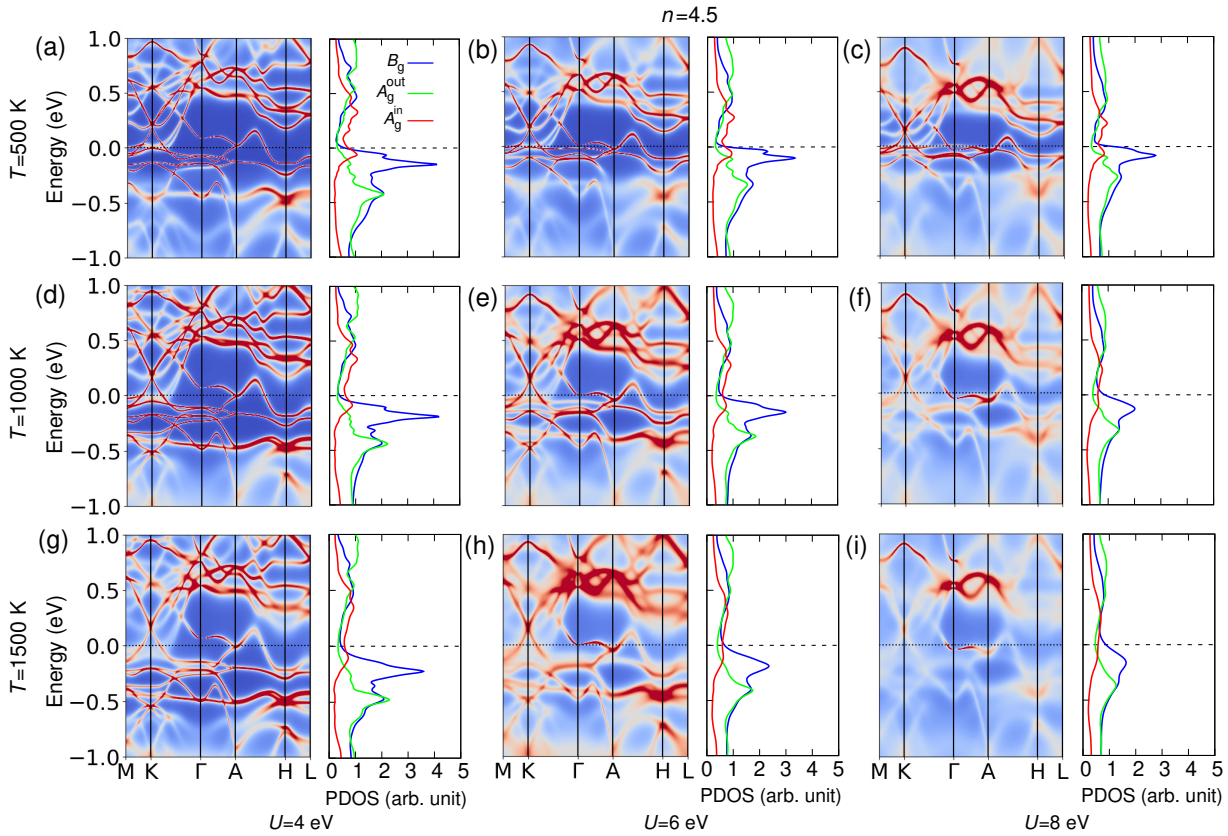

FIG. 6. Spectral function and PDOS computed from DMFT, using full Coulomb interaction for three sets of (U, J_H)=(4, 0.8), (6, 0.8), and (8, 0.8) eV and temperature T=500, 1000, and 1500 K for n = 4.5, respectively.

mean field theory and the density functional theory, Phys. Rev. Lett. **115**, 196403 (2015).

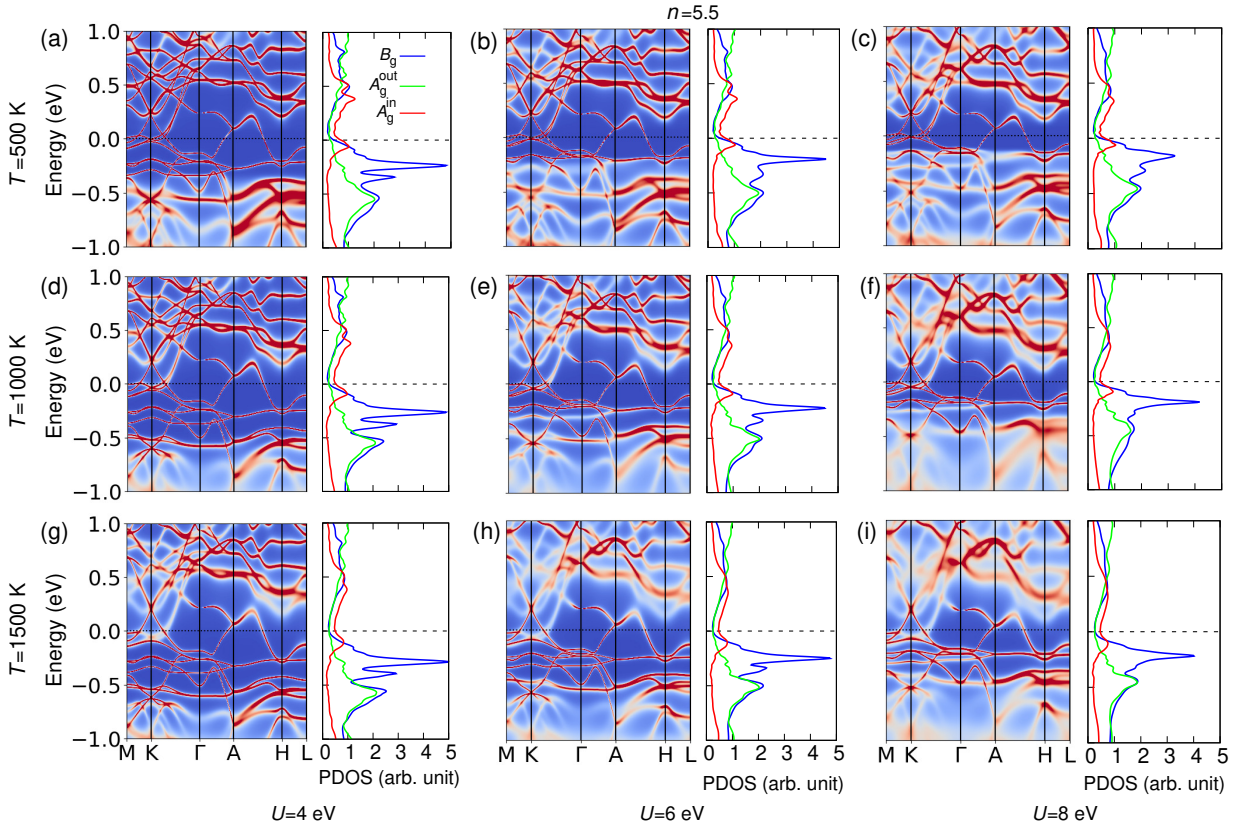

FIG. 7. Spectral function alongside PDOS obtained from DMFT calculations, employing full Coulomb interaction for $(U, J_{\rm H})$=(4, 0.8), (6, 0.8), and (8, 0.8) eV at T=500, 1000 and 1500 K, for n = 5.5, respectively.

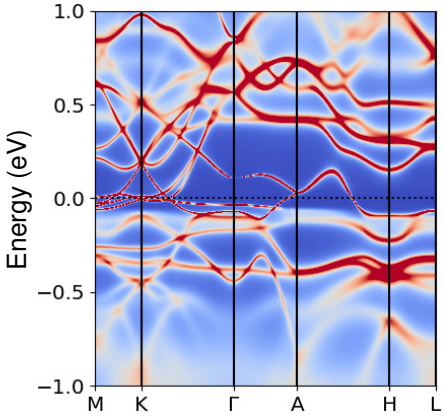

FIG. 8. Spectral function of SMAS obtained, using exact double scheme and full Coulomb interaction for $(U, J_{\rm H})$=(8, 0.8) eV at T=300 K.